Force Decomposition Analysis: A method to decompose intermolecular forces into physically relevant component contributions

Abdulrahman Aldossary,[†] Martí Gimferrer,[‡] Yuezhi Mao,[¶] Hongxia Hao,[†] Akshaya K. Das,[†] Pedro Salvador,[‡] Teresa Head-Gordon,[†] and Martin Head-Gordon[*,†]

[†] *Pitzer Center for Theoretical Chemistry, Department of Chemistry, University of California, Berkeley CA 94720, USA*

[‡]*Institut de Química Computacional i Catàlsi and Departament de Química, Universitat de Girona, 17003 Girona, Catalonia, Spain*

[¶] *Department of Chemistry and Biochemistry, San Diego State University, San Diego, CA 92182, USA*

E-mail: mhg@cchem.berkeley.edu

Abstract

Computational quantum chemistry can be more than just numerical experiments when methods are specifically adapted to investigate chemical concepts. One important example is the development of energy decomposition analysis (EDA) to reveal the physical driving forces behind intermolecular interactions. In EDA, typically the interaction energy from a good-quality density functional theory (DFT) calculation is decomposed into multiple additive components that unveil permanent and induced electrostatics, Pauli repulsion, dispersion, and charge-transfer contributions to non-covalent interactions. Herein, we formulate, implement and investigate decomposing the forces associated with intermolecular interactions into the same components. The resulting force decomposition analysis (FDA) is potentially useful as a complement to the EDA to understand chemistry, while also providing far more information than an

EDA for data analysis purposes such as training physics-based force fields. We apply the FDA based on absolutely localized molecular orbitals (ALMOs) to analyze interactions of water with sodium and chloride ions as well as in the water dimer. We also analyze the forces responsible for geometric changes in carbon dioxide upon adsorption onto (and activation by) gold and silver anions. We also investigate how the force components of an EDA-based force field for water clusters, namely MB-UCB, compare to those from force decomposition analysis.

1 Introduction

Intermolecular interactions are important for understanding chemistry as they affect structures, properties, and reactivity of chemical systems. Examples include red- or blue-shifts in vibrational frequencies when forming hydrogen bonds,[1–7] wavelength tuning of organic chromophores by the solvation or protein environment,[8–14] and modulation of the catalytic performance of molecular CO2RR catalysts through interactions with ligands in complexes' second coordination sphere.[15–22]

Decomposing the non-covalent interactions has been increasingly important to understanding the origins of these interactions as well as the development of classical force fields for the simulation of chemical and biochemical systems.[23–31] Moreover, to obtain statistical mechanical ensembles of a condensed phase chemical system, molecular dynamics simulations are required, for which accurate and efficient evaluation of intermolecular forces is important for systems where quantum chemical calculations are impractical.

Many energy decomposition analysis (EDA) methods have been proposed for separating different physical contributions to the non-covalent interaction energy, which are reviewed elsewhere.[32–38] In this work, we are using the absolutely localized molecular orbitals EDA (ALMO-EDA),[38–42] which divides the interaction energy into frozen (interaction between unrelaxed monomers), polarization (energy lowering due to intra-fragment relaxation of monomer wavefunctions), and charge transfer (energy lowering due to electron delocalization between fragments) contributions. The adiabatic EDA[43] optimizes the geometry successively on each of the intermediate potential energy surfaces (frozen, polarized, and fully relaxed), in essence attributing geometric changes and shifts in other molecular properties upon the formation of intermolecular complexes to the same terms as in ALMO-EDA. The adiabatic EDA has been successfully used to understand geometric changes arising from intermolecular interactions in a wide variety of systems.[6,43–48] For example, the ∠N-B-H angle in the ammonia-borane complex only bends when charge is allowed to flow from the ammonia to the borane molecule.[43,48] The adiabatic EDA thus attributes changes in *observables* to the different EDA contributions, which can be crucial for connecting to experimental results.

Many fixed-charge and polarizable force fields have been developed over the years for condensed-phase molecular simulations.[27–29,31,49–55] Recently, the T. Head-Gordon lab developed the MB-UCB many-body force field for water-water and water-ion interactions,[29,31] which employs terms that resemble those produced by ALMO-EDA of quantum mechanical calculations. For example, the polarization energy in the second-generation ALMO-EDA

allows electrons to move to the space of dipolar and quadrupolar density response to an external electric field, while MB-UCB uses distributed multipole analysis of classical anisotropic dipolar polarization to evaluate the polarization energy. Impressively, the two terms co-validate each other for a wide variety of water dimer geometries.[29] Similarly, the other terms are also related to each other as will be described below. While the total interaction energy and its breakdown given by MB-UCB and ALMO-EDA are in very good agreement, the forces remain to be compared to ensure the quality of dynamics driven by MB-UCB within a large ensemble of configurations.

In this work, we decompose the forces of an intermolecular interaction into constituent terms that directly correspond to those within the ALMO-EDA. After presenting the relevant theory, we demonstrate the usefulness of this decomposition for understanding chemistry with proof-of-concept examples of water interacting with sodium and chloride ions as well as the water dimer. We transform these forces to the internal coordinates using Wilson's B-matrix,[56] allowing us to see forces that are more intuitive and relatable to vibrational spectroscopy. For example, the H-O-H bending in the water molecule is used to understand the molecular environment.[57] We then study CO_2 adsorption and activation on Au and Ag anions and compare the two systems' forces within internal coordinates. The force decomposition is also applied to validate the forces produced by the MB-UCB force field. The force decomposition results, based on high-quality DFT calculations of the forces, may also be useful for future force-field training. This work builds on the adiabatic EDA to advance the idea of "property decomposition" analysis, in which not only the interaction energy is broken down, but also other derivatives of the energy, which are molecular properties. This general approach can be extended to the effect of intermolecular interactions on other properties of interest, such as the hessian matrix, NMR chemical shieldings, dipole moments or polarizabilities, etc. The observable changes in properties associated with non-covalent interactions can then be attributed to the different physical effects at play.

2 Theory

2.1 Energy Decomposition Analysis

In the ALMO-EDA, the total binding energy of an intermolecular complex is broken down into four components coming from the successive removal of constraints to minimize the energy of the supersystem:

$$\Delta E_{\text{bind}} = \Delta E_{\text{gd}} + \Delta E_{\text{frz}} + \Delta E_{\text{pol}} + \Delta E_{\text{ct}} \tag{1}$$

The geometry distortion term (ΔE_{gd}) refers to the energy consumed for each fragment to change its geometry from the equilibrium structure in isolation to that in the complex. The frozen (FRZ) interaction energy, ΔE_{frz}, is defined by the energy of the frozen wavefunction,[58] relative to that of the isolated non-interacting fragments (in distorted geometries). It corresponds to the energy change upon moving the isolated fragments into their positions in the complex while keeping their own electronic structure unchanged. The frozen wavefunction is the antisymmetric product of the isolated fragment wavefunctions, whose associated

one-particle density matrix (1PDM), $\mathbf{P}_{\text{frz}}$, is given by

$$\mathbf{P}_{\text{frz}} = (\mathbf{C}_o)_{\text{frz}} \boldsymbol{\sigma}_{\text{frz}}^{-1} (\mathbf{C}_o)_{\text{frz}}^T, \tag{2}$$

where $(\mathbf{C}_o)_{\text{frz}}$ is the direct sum of the (occupied) AO-to-MO coefficient matrices of the isolated fragments and $\boldsymbol{\sigma}_{\text{frz}}$ is the overlap matrix of the orbitals coming from the $(\mathbf{C}_o)_{\text{frz}}$ matrix. This 1PDM definition gives us the frozen interaction energy definition:

$$\Delta E_{\text{frz}} = E[\mathbf{P}_{\text{frz}}] - \sum_A E[\mathbf{P}_A]. \tag{3}$$

The next contribution, the polarization energy (ΔE_{pol}), arises from allowing the occupied orbitals on each fragment to mix with the virtuals *only* on the same fragment. Minimizing the energy subject to this constraint, also known as the SCF-MI procedure,[59–63] leaves the AO-to-MO coefficient matrix still block-diagonal and the corresponding MOs "absolutely localized" on each fragment while also polarized in the presence of each other. The resulting electronic wavefunction is referred to as the polarized state, whose 1PDM is denoted as $\mathbf{P}_{\text{pol}}$. The polarization energy is then defined as the energy lowering of the polarized state relative to the frozen state:

$$\Delta E_{\text{pol}} = E[\mathbf{P}_{\text{pol}}] - E[\mathbf{P}_{\text{frz}}]. \tag{4}$$

Since the polarization density comes from variationally minimizing the energy, ΔE_{pol} is negative semi-definite. Lastly, by removing the ALMO constraint, we obtain the fully relaxed state for the intermolecular complex. The energy lowering due to electron delocalization is defined as the charge transfer term (ΔE_{ct}):

$$\Delta E_{\text{ct}} = E[\mathbf{P}_{\text{full}}] - E[\mathbf{P}_{\text{pol}}], \tag{5}$$

where $\mathbf{P}_{\text{full}}$ is the 1PDM for the fully relaxed state.

2.2 Force Decomposition Analysis

Within a variational EDA scheme like the ALMO-EDA, the analytic nuclear forces associated with each of the intermediate (including the initial and final) states can be obtained. Following the derivations in our previous work,[43] namely the adiabatic EDA scheme where the nuclear forces were used to optimize the complex geometry on the frozen, polarized, and fully relaxed surfaces, here we introduce the ALMO-based force decomposition analysis (FDA) method, where the nuclear derivatives of the frozen (ΔE_{frz}), polarization (ΔE_{pol}), and charge transfer (ΔE_{ct}) components of the interaction energy, as well as that of the classical electrostatics component of the frozen interaction ($\Delta E_{\text{cls-elec}}$), are obtained. Note that many of the derivations here can be applied to other variational EDA schemes.

Just as ALMO-EDA decomposes an interaction energy, the ALMO-based FDA decomposes *intermolecular forces* into frozen, polarization, and charge transfer components:

$$\Delta \mathbf{F}_{\text{int}} = \Delta \mathbf{F}_{\text{frz}} + \Delta \mathbf{F}_{\text{pol}} + \Delta \mathbf{F}_{\text{ct}} \tag{6}$$

The frozen component of the intermolecular forces ($\Delta \mathbf{F}_{\text{frz}}$) can be obtained by differen-

tiating Eq. (3) with respect to the nuclear coordinates:

$$\Delta \mathbf{F}_{\text{frz}} = \mathbf{F}_{\text{frz}}[\mathbf{P}_{\text{frz}}] - \sum_A \mathbf{F}_A[\mathbf{P}_A] \tag{7}$$

where $\mathbf{F}_{\text{frz}}$ denotes the forces on the frozen PES, and the term being subtracted on the right-hand side is the collection of isolated fragment forces that arises from the distortion of fragment structures within the complex. Note that these isolated fragment forces can be compared to the nuclear derivatives of the bonded terms in molecular mechanical force fields, while in this work we focus on the intermolecular force components. With superscripts "x" signifying derivatives with respect to the x-th nuclear coordinate (and superscripts "$\mathbf{S}$" and "$\boldsymbol{\Delta}_A$" in the same fashion), based on the derivation in our previous work,[43] the x-th component of forces on the frozen surface, $(F_{\text{frz}})_x$, is given by

$$(F_{\text{frz}})_x = - \left[V_{\text{nn}}^x + \mathbf{P}_{\text{frz}} \cdot \mathbf{h}^x + \frac{1}{2} \mathbf{P}_{\text{frz}} \cdot \ \mathbf{II}^x \cdot \mathbf{P}_{\text{frz}} + E_{\text{xc}}^x + E_{\text{frz}}^{\mathbf{S}} \cdot \mathbf{S}^x + \sum_A \left(E_{\text{frz}}^{\boldsymbol{\Delta}_A} \cdot \boldsymbol{\Delta}_A^x \right) \right], \tag{8}$$

where V_{nn} is the nuclear-nuclear coulomb repulsion potential, $\mathbf{h}$ is the core Hamiltonian (kinetic energy and nuclei-electron attractions), II is the AO two-electron integrals, E_{xc} is the Kohn-Sham (KS) exchange-correlation energy, $\mathbf{S}$ is the AO overlap matrix, and $\boldsymbol{\Delta}_A$ is the matrix of occupied-virtual orbital rotations (variational parameters) within a given fragment. The first four terms are identical to those in the KS-DFT nuclear forces, while the last two terms require treatments that are specific to the frozen PES. The reader is referred to Ref. 43 for details.

Similarly, the polarization contribution to the intermolecular forces can be evaluated by differentiating Eq. (4):

$$\Delta \mathbf{F}_{\text{pol}} = \mathbf{F}_{\text{pol}}[\mathbf{P}_{\text{pol}}] - \mathbf{F}_{\text{frz}}[\mathbf{P}_{\text{frz}}] \tag{9}$$

The derivation of $\mathbf{F}_{\text{pol}}$ depends on the definition of fragment polarization subspaces in the SCF-MI calculation,[64] i.e., the degrees of freedom for each fragment's occupied-virtual mixing to occur. In the simplest case where the full AO space of each fragment is active in the polarization (SCF-MI) calculation as in the 1st-generation ALMO-EDA,[39] $\mathbf{F}_{\text{pol}}$ has a similar expression to Eq. (8) except that the last term vanishes due to the stationary condition of SCF-MI ($E_{\text{pol}}^{\boldsymbol{\Delta}_A} = \mathbf{0}$):

$$(F_{\text{pol}})_x = - \left[V_{\text{nn}}^x + \mathbf{P}_{\text{pol}} \cdot \mathbf{h}^x + \frac{1}{2} \mathbf{P}_{\text{pol}} \cdot \ \mathbf{II}^x \cdot \mathbf{P}_{\text{pol}} + E_{\text{xc}}^x + E_{\text{pol}}^{\mathbf{S}} \cdot \mathbf{S}^x \right] \tag{10}$$

Note that in this simplest case, $E_{\text{pol}}^{\mathbf{S}}$ has an identical form to that in the standard SCF energy gradient.[43] Finally, the charge-transfer contribution to the intermolecular forces can be obtained by differentiating Eq. (5):

$$\Delta \mathbf{F}_{\text{ct}} = \mathbf{F}_{\text{full}}[\mathbf{P}_{\text{full}}] - \mathbf{F}_{\text{pol}}[\mathbf{P}_{\text{pol}}] \tag{11}$$

where $\mathbf{F}_{\text{full}}$ stands for the standard KS-DFT forces for the fully relaxed complex.

The frozen interaction term in ALMO-EDA comprises contributions from permanent elec-

5

trostatics, Pauli repulsion, and dispersion.[65] To improve the interpretability of FDA results and to facilitate comparison with terms in polarizable force fields, here we introduce how one can evaluate forces arising from "quasi-classical" electrostatics ($\Delta \mathbf{F}_{\text{cls-elec}}$), i.e., coulomb interactions between charge distributions (nuclei and electrons) of different fragments, which can be employed to benchmark forces arising from permanent charge and multipole interactions in a force field. The remainder of $\Delta \mathbf{F}_{\text{frz}}$ then incorporates contributions from the non-electrostatic components of the frozen interaction (Pauli repulsion and dispersion), which we refer to as the van der Waals (vdW) contribution since it corresponds roughly to the sum of attractive and repulsive vdW potential in a force field:

$$\Delta \mathbf{F}_{\text{frz}} = \Delta \mathbf{F}_{\text{cls-elec}} + \Delta \mathbf{F}_{\text{vdw}} \tag{12}$$

The quasi-classical electrostatic interaction among N fragments can be expressed in the following compact form:

$$\Delta E_{\text{cls-elec}} = \frac{1}{2} \sum_{A \neq B}^{N} \left[\mathbf{P}_A \cdot \mathbf{V}_{\text{ee+en}}^{B} + V_{\text{nn}}^{AB} \right] \tag{13}$$

where $\mathbf{P}_A$ is the AO-basis 1PDM of isolated fragment A, $\mathbf{V}_{\text{ee+en}}^{B}$ is the coulomb potential (nuclear and electronic) arising from fragment B, also in the AO basis, and V_{nn}^{AB} is the nuclear-nuclear repulsion potential between fragments A and B. Differentiating Eq. (13) yields

$$(\Delta F_{\text{cls-elec}})_x = -\frac{1}{2} \sum_{A \neq B} \left[(\mathbf{P}_A)^x \cdot \mathbf{V}_{\text{ee+en}}^{B} + \mathbf{P}_A \cdot (\mathbf{V}_{\text{ee+en}}^{B})^x + (V_{\text{nn}}^{AB})^x \right], \tag{14}$$

where the derivative of isolated fragment density $\mathbf{P}_A$ can be further expanded based on its dependence on fragment A's AO overlap matrix ($\mathbf{S}_A$) and occupied-virtual orbital rotation ($\mathbf{\Delta}_A$):

$$(\mathbf{P}_A)^x = \mathbf{P}_A^{\mathbf{S}_A} \cdot (\mathbf{S}_A)^x + \mathbf{P}_A^{\mathbf{\Delta}_A} \cdot (\mathbf{\Delta}_A)^x \tag{15}$$

Note that the detailed forms of $\mathbf{P}_A^{\mathbf{S}_A}$ and $\mathbf{P}_A^{\mathbf{\Delta}_A}$ have been derived in our previous work.[43,66] For completeness here we show the mathematical details regarding these two derivatives in SI Sec. S1.

2.3 The MB-UCB Force Field

The MB-UCB force field[29,31] was developed based on the principles of the many-body expansion combined with ALMO-EDA variational energy decomposition analysis for each of the terms of the total intermolecular energy

$$E_{\text{inter}} = E_{\text{elec}} + E_{\text{pol}} + E_{\text{CT}} + E_{\text{disp}} + E_{\text{Pauli}} \tag{16}$$

This advanced non-reactive force field introduced anisotropic atomic polarizability of the water molecule,[67] as well as explicit treatment of charge transfer and charge penetration contributions for both water and aqueous alkali metal and halogen ions.[29,31]

The permanent electrostatics for the MB-UCB force field uses atom centered point mul-

tipoles

$$E_{\text{elec}} = \sum_{i<j} \mathbf{M}_i^T \mathbf{T}_{ij} \mathbf{M}_j \tag{17}$$

where $\boldsymbol{M}_i^T$ is the multipole coefficient vector and T_{ij} is the multipole interaction tensor that consists of appropriate associated derivatives of $1/r_{ij}$. The monopole-monopole term is modified to describe charge penetration (CP) via separation of the atomic charge into a core nuclear charge, Z_i and smeared electron cloud charge $Z - q_i$. Hence the modified charge-charge electrostatic interactions between two atoms A and B with atomic charges q_A and q_B are expressed as

$$\begin{aligned} E_{\text{elec}}^{q-q} =& \frac{Z_A Z_B}{r} - \frac{Z_A (Z_B - q_B)}{r} f_{\text{damp}} - \frac{Z_B (Z_A - q_A)}{r} f_{\text{damp}} \\ &+ \frac{(Z_A - q_A)(Z_B - q_B)}{r} f_{\text{damp}}^{\text{overlap}} \end{aligned} \tag{18}$$

The two damping functions,

$$\begin{aligned} f_{damp} &= (1 - \exp(-\alpha r)) \\ f_{damp}^{overlap} &= (1 - exp(-\beta_A r))(1 - exp(-\beta_B r)) \end{aligned} \tag{19}$$

require two parameters, α and β, to control the damping of core–electron and electron–electron interactions, respectively, in order for the charge penetration effects to vanish rapidly and to recover the classical Coulombic multipolar interactions at longer distances. We use the CP model parameterization due to Piquemal and co-workers.[68]

Many-body polarization is explicitly incorporated by point induced dipoles, μ_{ind}, at each atomic center[49]

$$\boldsymbol{\mu}_i^{\text{ind}} = \alpha_i \left[\sum_j \mathbf{T}_{ij} \mathbf{M}_j - \sum_{j \neq i} \mathbf{T}_{ij}^{\text{d-d}} \boldsymbol{\mu}_j^{\text{ind}} \right] \tag{20}$$

where α_i is the atomic polarizability and $\mathbf{T}_{ij} \mathbf{M}_j$ formulates the permanent electric field. T_{ij}^{d-d} is the dipole-dipole interaction tensor in which the off-diagonal blocks of T_{d-d} are Thole damped[69] Cartesian interaction tensors between induced dipoles of two polarizable sites i and j. Unlike other polarizable force fields such as AMOEBA and AMOEBA+ that use rotationally invariant isotropic atomic polarizabilities[28,53,70], MB-UCB uses a rank two anisotropic atomic polarizablity tensor. The polarization energy can expressed in terms of induced dipoles as

$$E_{\text{pol}} = -\frac{1}{2} \sum_i \boldsymbol{\mu}_i^{\text{ind}} \mathbf{E}_i \tag{21}$$

and the induced dipoles at each multipole site are obtained by solving Equation 20 self-consistently.[71,72]

MB-UCB uses an empirical many-body function similar to the polarization energy induced multipoles to incorporate the many-body charge transfer energy.[73]

$$E_{\text{CT}-\text{ind}} = -\frac{1}{2} \sum_i \mu_i^{\text{ct}-\text{ind}} \mathbf{E}_i^{\text{ct}}$$

$$\boldsymbol{\mu}_i^{\text{ct}-\text{ind}} = \alpha_i^{\text{ct}} \left[\sum_j \mathbf{T}_{ij}^{\text{ct}} \mathbf{M}_j - \sum_{j \neq i} \mathbf{T}_{ij}^{\text{ct}[\text{d}-\text{d}]} \boldsymbol{\mu}_j^{\text{ct}-\text{ind}} \right] \tag{22}$$

where α_i^{ct} controls the charge transfer energy between two multipole sites through a response to the permanent electrostatics, and the multipole interaction matrix (T^{ct}) elements are damped with an exponential damping function.

$$\mathbf{T}_\zeta^{\text{ct}} = - \left[1 - d \exp\left(-b u^3\right) \right] \frac{r_\zeta}{r_{ij}^3}, \quad \zeta = x, y, z \qquad u = \frac{r_{ij}}{\left(\alpha_i^{\text{ct}} \alpha_j^{\text{ct}}\right)^{1/6}} \tag{23}$$

The three parameters α_{ct}, b and d are responsible for the fast exponential decay of the charge transfer energy, which should be more short-ranged than polarization.[29,31]

The remaining energy terms are Pauli repulsion and dispersion, and are modeled in MB-UCB as a van der Waals interaction using a buffered 14-7 pairwise-additive function proposed by Halgren[74] and utilized in all AMOEBA force fields.[49,53,70]

$$E_{\text{vdW}} = \sum_{i<j} \epsilon_{ij} \left(\frac{1+\delta}{\sigma_{ij} + \delta} \right)^7 \left(\frac{1+\gamma}{\sigma_{ij}^7 + \gamma} - 2 \right) \tag{24}$$

where ϵ defines the energy scale, $\sigma = R_0/r$ is the distance between two atoms, and R_0 is the distance corresponding to the minimum energy. Like AMOEBA,[75] we set the two constants δ and γ to 0.12 and 0.07, respectively. Given the total functional forms of the energy terms of MB-UCB, the corresponding force terms are easily defined through the usual chain rule formulations and easily compared to the FDA analysis proposed here.

2.4 Computational details

The force decomposition analysis method discussed here was implemented in a developer version of Q-Chem 5.[76] The geometries used for molecular calculations were optimized and run at the ωB97X-D[77]/def2-TZVPPD[78] level of theory, with exception to the gold/silver CO_2 complex, where ωB97X-V[79] density functional instead along with the appropriate def2-ECP.[80] To diagnose the atomic forces of MB-UCB, we use the same level of theory used in the original paper,[29] namely ωB97X-V[79]/def2-QZVPPD.[78] DFT numerical integration was performed on (99,590) grid for XC functional and SG-1[81] for non-local correlation. All geometries are included in the Supplementary Material (SI).

Fifty water dimer geometries were used to compare the atomic force contributions between FDA and MB-UCB. The geometries were taken from the iAMOEBA training data set,[51] where pairs of molecules were randomly picked from AMOEBA liquid water simulation between 257.15 - 373.15 K such that it is representative of a wide range of the phase space. The geometries are provided in the supplementary information.

Forces are turned into internal coordinates by a linear transformation using the pseudo-inverse of Wilson's B matrix.[56,82,83] The B matrix was generated using Q-Chem 5[76] with a minor modification of connecting intra-fragment atoms first and then minimally connecting

the inter-fragment atoms to avoid non-intuitive bonds and angles. Details are included in SI Sec. S2

3 Results and discussion

3.1 $H_2O \cdots Na^+$, $Cl^- \cdots HOH$ and the water dimer

First we look at the water molecule interacting with an innocent cation, Na^+, and a simple anion, Cl^-. Aside from the importance of these examples in understanding water-ion interactions, they will illustrate the nature of the FDA information, as well as its representation in internal coordinates. We use geometries where the position of the ion is optimized relative to a water molecule constrained to its isolated geometry. This is a convenient choice because $\mathbf{F}_{tot} = \Delta \mathbf{F}_{int}$ since $\mathbf{F}_A = \mathbf{0}$ for $A = H_2O$. As a result, the interfragment degrees of freedom will have zero net force, as well as zero resultant force in the FDA in order to see how the FDA components cancel each other out. By contrast, there will be nonzero $\Delta \mathbf{F}_{int}$ for intramolecular degrees of freedom, which will indicate how such internal coordinates will deform in a fully optimized complex. The FDA will reveal which component contributions are primarily responsible for such changes.

At equilibrium, the Na^+–O vector is aligned with the water dipole vector, optimizing the charge-dipole interaction. With C_{2v} symmetry, there are only three non-redundant internal coordinates, namely O–H, O–Na, and ∠HOH. The FDA is shown in the left panel of Fig. 1. By far the most interesting result is $\Delta \mathbf{F}_{int}(O - Na^+)$, which is overall zero, as a result of a strong force of extension due to Pauli repulsion (the van der Waals term in Fig. 1) being compensated by an equally strong force of contraction due to electrostatic attraction. The electrostatic attraction force is about 80% due to the permanent electrostatics, and only 20% due to polarization (of water by Na^+). There is negligible contribution from charge transfer, emphasizing the innocent nature of Na^+ as an ineffective Lewis acid. The O–H bonds are remote from Na^+, so the forces distorting the optimal monomer geometry in the complex are small. The largest formation force is $\Delta \mathbf{F}_{int}(O - H)$, which has a small force of extension driven by polarization. We can understand this effect as a result of promotion of a fraction of an electron from the σ_{OH} orbitals to antibonding orbitals, presumably with σ_{OH}^* character.
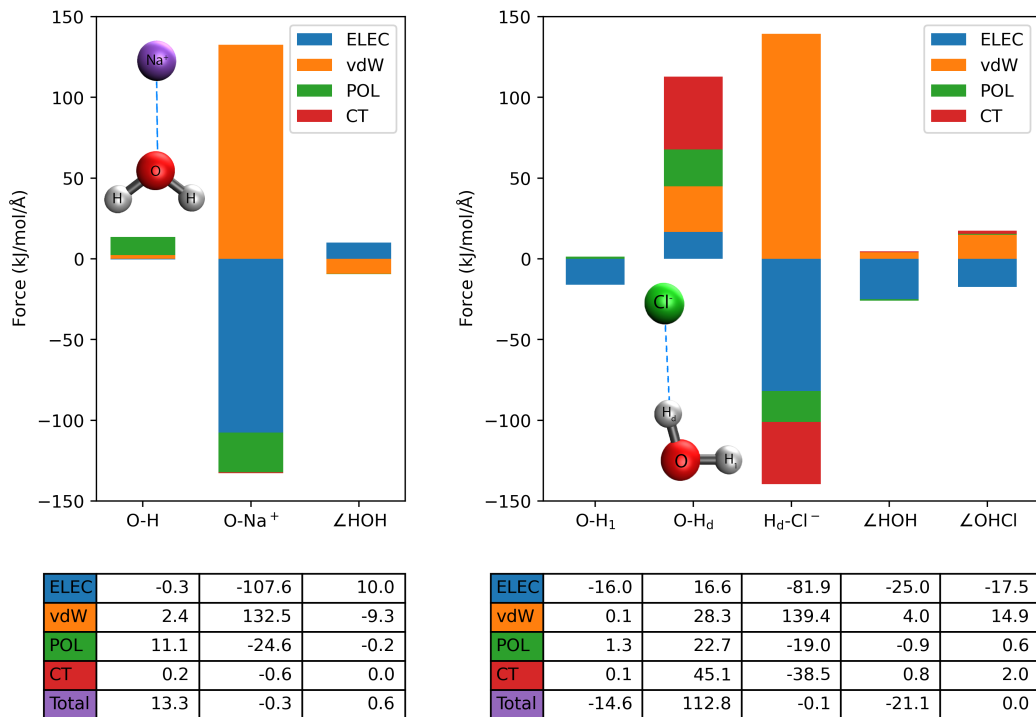
9

Figure 1: FDA results in the internal coordinates for H_2O interacting with Na^+ (left) and Cl^- (right). These forces are evaluated at the PES minima, keeping the water molecule at its isolated geometry. The tables at the bottom replicate the data with numbers for easier comparison.

FDA for the hydrogen bonded complex formed between water and the chloride anion, as given in the right panel of Fig. 1, presents an interesting contrast with the $H_2O \cdots Na^+$ case, which was previously analyzed by the ALMO-EDA.[66,84] Despite on-going debate,[85–89] it is fairly well-established that hydrogen-bonds involve significant contributions from permanent and induced electrostatics, and charge transfer,[40,43,89] in competition with Pauli repulsion. Focusing first on the inter-fragment $H_d - Cl^-$ force, which is optimized to zero, we see three forces of contraction (permanent electrostatics > charge transfer > polarization) balanced by the extension force due to Pauli repulsion. From a force equilibrium perspective, this very nicely illustrates the "driving forces" that give rise to the hydrogen bond. The other interfragment coordinate, $\angle OH_dCl$, is optimized as a balance between permanent electrostatics (attempting to shrink the angle), and Pauli repulsion (attempting to enlarge the angle). This competition is controlled by the frozen part of the interaction energy, as previously noted for the water dimer.[43] Within the water molecule, there is a strong force of extension along the OH_d bond. Its primary origin is charge transfer, followed by Pauli repulsion, induced electrostatics and permanent electrostatics. Both CT and polarization can be readily understood in terms of partial occupation of the $\sigma^*_{OH_d}$ orbitals.
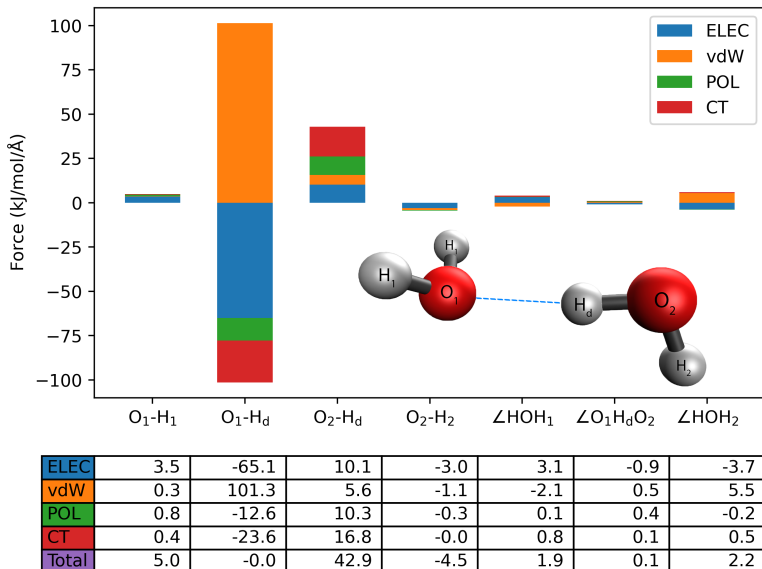
10

Figure 2: FDA results in the internal coordinates for the water dimer at the minimum-energy distance, with the monomers fixed in their isolated geometries. The table at the bottom replicates the data with numbers for easier comparison.

	O_1-H_1	O_1-H_d	O_2-H_d	O_2-H_2	$\angle HOH_1$	$\angle O_1H_dO_2$	$\angle HOH_2$
ELEC	3.5	-65.1	10.1	-3.0	3.1	-0.9	-3.7
vdW	0.3	101.3	5.6	-1.1	-2.1	0.5	5.5
POL	0.8	-12.6	10.3	-0.3	0.1	0.4	-0.2
CT	0.4	-23.6	16.8	-0.0	0.8	0.1	0.5
Total	5.0	-0.0	42.9	-4.5	1.9	0.1	2.2

Next, we examine FDA for the hydrogen-bonded water dimer, as shown in Fig. 2; this system has also been carefully analyzed previously by the ALMO-EDA.[66,87] The zero net force on the hydrogen-bond coordinate, O_1H_d, shows the FDA view of this characteristic hydrogen-bond interaction. Classical electrostatics dominates the forces seeking to further shorten the hydrogen bond, consistent with force-field viewpoints. Intermolecular charge transfer is the second strongest force of contraction, followed by polarization. Pauli repulsion provides an exactly balancing force of extension. Within the proton-donor water molecule (which of course is the electron pair acceptor), the intramolecular O_2H_d bond constrained to the geometry of the free water molecule experiences a force of extension to which all components contribute with the same sign. Similar to the water-chloride complex, charge transfer and polarization partially occupy the antibonding $\sigma^*_{OH_d}$ orbitals and are the leading drivers of O_2H_d bond elongation.

3.2   Assessing force components of an advanced water force field

Generating the force vectors corresponding to each energy term in the ALMO-EDA yields a greatly augmented set of data at each geometry. Such data can in principle be employed to aid in the development or validation of advanced force fields, perhaps in conjunction with powerful existing tools such as Force Balance[70,90] or machine learning.[91,92] To illustrate the use of FDA data, we assess the forces that are obtained from a recently reported force field for water, MB-UCB.[29] Although the energies of MB-UCB have already shown to be in excellent agreement with ALMO-EDA,[29] no comparable assessment of the decomposed forces has yet been done, although total and force components of the complete energy derivative have been assessed for other force fields such as iAMOEBA[51] and AMOEBA14[53] to which

we compare below. The term-by-term force contributions from the FDA against MB-UCB has been assessed for a set of 50 water dimer geometries extracted from finite temperature MD trajectory as described in the computational details section. For these snapshots, the ALMO-EDA energy components and the corresponding contributions for MB-UCB, shown in SI Sec. S3, show excellent agreement, as expected based on our previous work.[29]

We begin our assessment by comparing the FDA and MB-UCB force components on the center of mass (CoM) of each water molecule in the data set broken down by interaction. The COM forces are a sum of all atomic forces on a molecule, also referred to as molecular forces or net forces.[51,93] The results are shown as correlation plots in Fig. 3 in which the RMS error in the total CoM force is ~ 8 kJ/mol/Å. This is a reasonably small error when considering the fact that a DFT geometry optimization is considered converged at a maximum force of ~ 1-2 kJ/mol/Å, and is comparable to the ~ 10 kJ/mol/Å RMS error in AMOEBA and iAMOEBA forces versus ab initio forces reported for water clusters.[51,53] Perhaps the most important point that emerges from Fig. 3 is the fact that the RMSD in each non-bonded
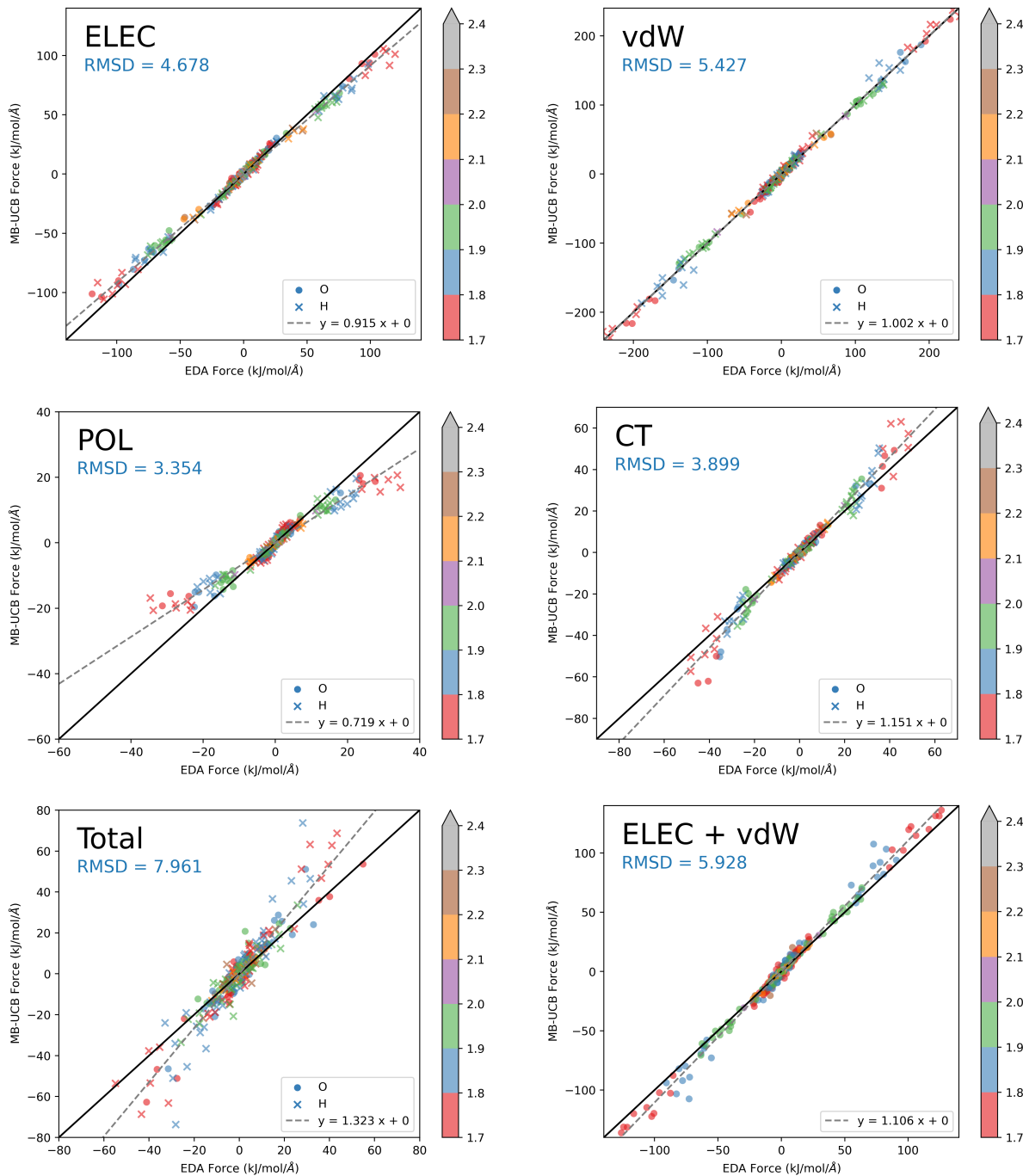
Figure 3: *Correlation between FDA decomposed forces and the corresponding MB-UCB forces on the centers of mass of each water molecule for a sample of 50 water dimer geometries. The force decompositions considered are electrostatics (ELEC), van der Waals (vdW), polarization (POL), and charge transfer (CT), and the total intermolecular interaction (TOT). The color bins indicate the distance to the closest atom of the other fragment, i.e., small numbers indicate the dimer is in the compressed region. The equilibrium water dimer closest contact atoms sit at 1.9 Å, which corresponds to the data points colored in blue. The dashed line corresponds to a least squares fit of the errors, where the line fit equation is shown in the legend of each plot.*

contribution to the MB-UCB CoM force is smaller than the RMSD in the MB-UCB total force. Even the very large ELEC and vdW forces exhibit RMSD values of only 4.7 and 5.4 kJ/mol/Å, respectively. The largest deviations are associated with the largest forces, as expected, where short-range damping, such as Thole damping of polarization,[69] are likely to exert an influence. Overall, we can conclude that the decomposed contributions to the CoM forces via MB-UCB are as good or better behaved than the total MB-UCB CoM forces.

A more stringent FDA test is to assess the errors in the Cartesian forces on each atom, for which a correlation plot between the FDA and MB-UCB decompositions is shown in Fig. 4. The overall RMSD value is increased by only ∼10% for the atomic forces vs the CoM forces, rising to ∼8.8 kJ/mol/Å, which is encouragingly good performance when compared to iAMOEBA or AMOEBA, in which atomic forces showed RMS errors more than twice as large as CoM forces.[51] Although the RMS of the ELEC atomic forces increases relative to the COM electrostatic forces, they are still comparable to the total atomic force errors.

However, the vdW term shows a significantly larger atomic force error compared to the total or COM force error. It is pertinent to mention that MB-UCB situates the vdW centers for the hydrogen atoms at a fixed fraction (0.91) of the OH bond length, rather than at the atomic centers themselves. Hence the virtual site forces must be redistributed over the particles with mass in a consistent way, which only guarantees that the total force is preserved, and may explain some of the vdW force deviations observed. Even so, there is some error cancellation between ELEC and vdW atomic forces as seen in the ELEC+vdW plot in Fig. 4, which was not the case in the CoM force components. Finally, the more challenging nature of the atomic force components (and the total atomic force) is also evident in the fact that the largest errors no longer occur predominantly at the largest absolute force values. Fig. 4 shows RMS errors when either MB-UCB predicts near zero atomic forces compared to finite FDA forces (such as for POL or CT) or that finite MB-UCB atomic forces are found when FDA forces are near zero (for example, vdW).
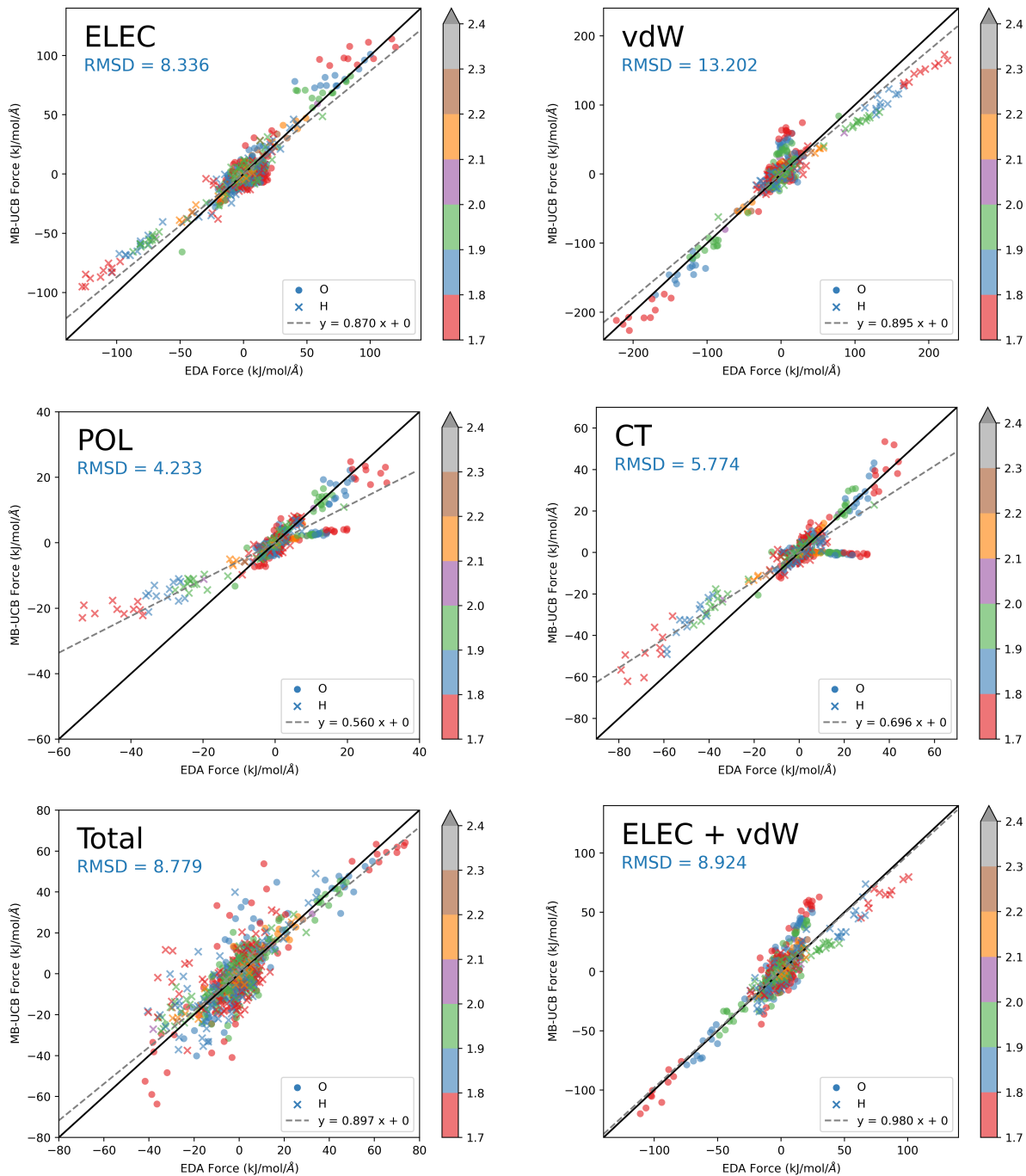
Figure 4: *Correlation between FDA decomposed component forces and the corresponding MB-UCB forces on the atomic centers of each water molecule for a sample of 50 water dimer geometries.* Other details are as defined in Fig. 3.

One more way to compare MB-UCB forces against the FDA results, is to separately evaluate the RMS deviations in the total CoM force (left panel) and the atomic forces (right panel) as a function of the closest intermolecular distance in Fig. 5. These plots make it clear that errors decay rapidly as a function of intermolecular separation. The plots also serves

to emphasize the fact that the quality of the individual MB-UCB decomposed CoM force is statistically better than the MB-UCB total force. On the other hand, at intermolecular distances of 2 Å and shorter, errors in the MB-UCB vdW force contribution are larger than the total MB-UCB RMSD; in other words, there is partial error compensation with the ELEC term in particular. It is encouraging that the errors associated with the MB-UCB description of charge transfer and polarization contributions remain relatively low even in the compressed region for both the atomic force and CoM force, although their magnitude increases with the reduction of the closest contact distance. The CT term shows more scope for improvement, which is likely to be a result of the less physically appropriate form that was employed within MB-UCB.[29]
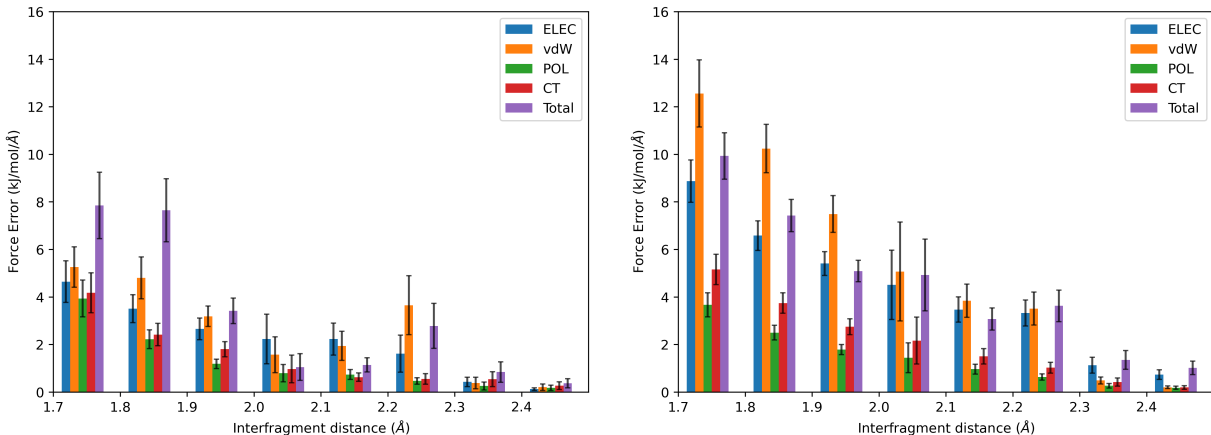

Figure 5: *Mean absolute deviations in the total CoM force (left panel) and the atomic forces (right panel) as a function of the closest intermolecular distance.* The mean errors in MB-UCB forces plotted against the closest contact between the two water molecules broken down into the non-bonded components of interaction. The left panel applies to the CoM force on each water molecule, while the right panel applies to the atomic forces. Values plotted are the RMSDs for all data points within each 0.1 Å bin of closest intermolecular distance. The error bars indicate 95% confidence interval.

3.3   Interaction of CO_2 with Au^- and Ag^-

The reduction of CO_2 to $CO_2^{\bullet-}$ is the first step on the pathway towards conversion of CO_2 into fuels, of which the simplest is 2-electron reduction to CO_2.[94] The reverse reaction, CO oxidation to CO_2, is also well-studied.[95] At the level of model systems, negatively charged gold oxide clusters have been shown to react with CO to yield CO_2,[96] via reactions as simple as $AuO^- + CO \longrightarrow Au^- + CO_2$. The exit channel complex, $[Au \cdots CO_2]^-$, has been studied as part of that reaction,[96] as well as characterized by separate experiments and computations.[97–99] Remarkably, as shown in Fig. 6(a) and (b), there are two local minima in the exit channel: a strongly bound chemisorbed structure, which exhibits significant activation (i.e., reduction) of the CO_2 ($\angle OCO = 143°$), and a physisorbed complex where CO_2 is not activated ($\angle OCO = 172°$).
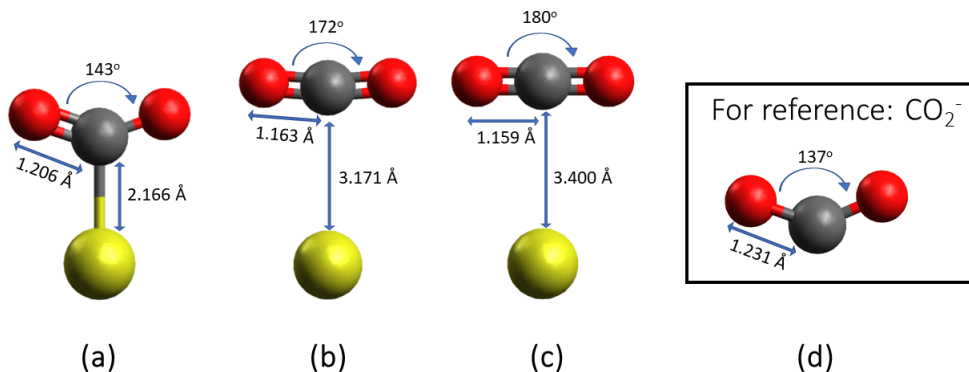
16

Figure 6: A diagram showing the different configurations of the Au^-CO_2 with the labeled bond distances and angles; due to C_{2v} symmetry, there are only 3 non-redundant internal coordinates, which are the Au–C distance, the C–O bond length, and the CO_2 bending coordinate. (a) the chemisorbed species at $R(AuC) \sim 2.2$ Å, (b) the physisorbed species at $R(AuC) \sim 3.2$ Å, (c) a constrained geometry ($R(AuC)$ optimized with CO_2 fixed at its optimal isolated geometry) exhibiting a minimum at $R(AuC) \sim 3.4$ Å, (d) the charged anion of $CO_2^{\bullet -}$.

On the other hand, the silver anion was reported experimentally to exhibit only the physisorbed species,[99] perhaps reflecting the smaller size of the gold atom compared to silver due to relativistic contraction. We show a fully relaxed potential energy scan along the M–C distance with the energy decomposition analysis results in Fig. 7. General agreement with the experimental facts is evident in the PES scan. The size effect is already clear with Ag showing more repulsive van der Waals interactions (sum of Pauli repulsion and dispersion) at 4 Å and stronger electrostatic attraction than Au. Despite charge transfer being a dominant contribution to the interaction, CT is very comparable for Au and Ag at shorter M–C distances, although Ag's CT is stronger than Au's at longer distances due to size. With an ionization energy of only 126 kJ/mol,[100] Ag^- is a stronger electron donor (Lewis base) than Au^-, whose ionization energy is 223 kJ/mol.[101]
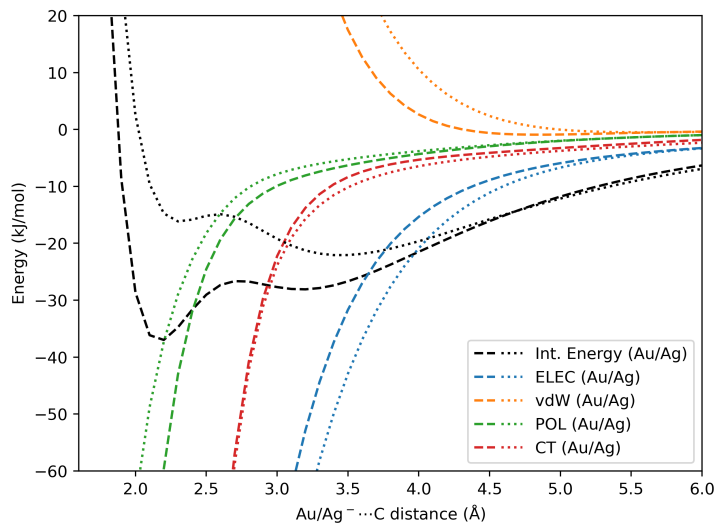
Figure 7: Fully relaxed potential energy surface scans (kJ/mol) for Au^-CO_2 (black dashes) and Ag^-CO_2 (black dots) with the EDA components (dashes for Au^-CO_2 and dots for Ag^-CO_2).

Next, we look into the forces for both the physisorbed and chemisorbed species. For easier comparison, we take the geometries of two minima for the gold complex and use these same geometries for silver. Since the CO_2 molecule in these geometries is distorted compared to the isolated molecule, we will refer to that difference in energy as a preparation (Prep) energy. Similarly, we refer to the forces that arise from the preparation energy (which will cause the CO_2 to relax back to its isolated geometry) as the preparation force. The FDA results at the physisorbed geometry are shown in Fig. 8, while results at the chemisorbed geometry are shown in Fig. 9.
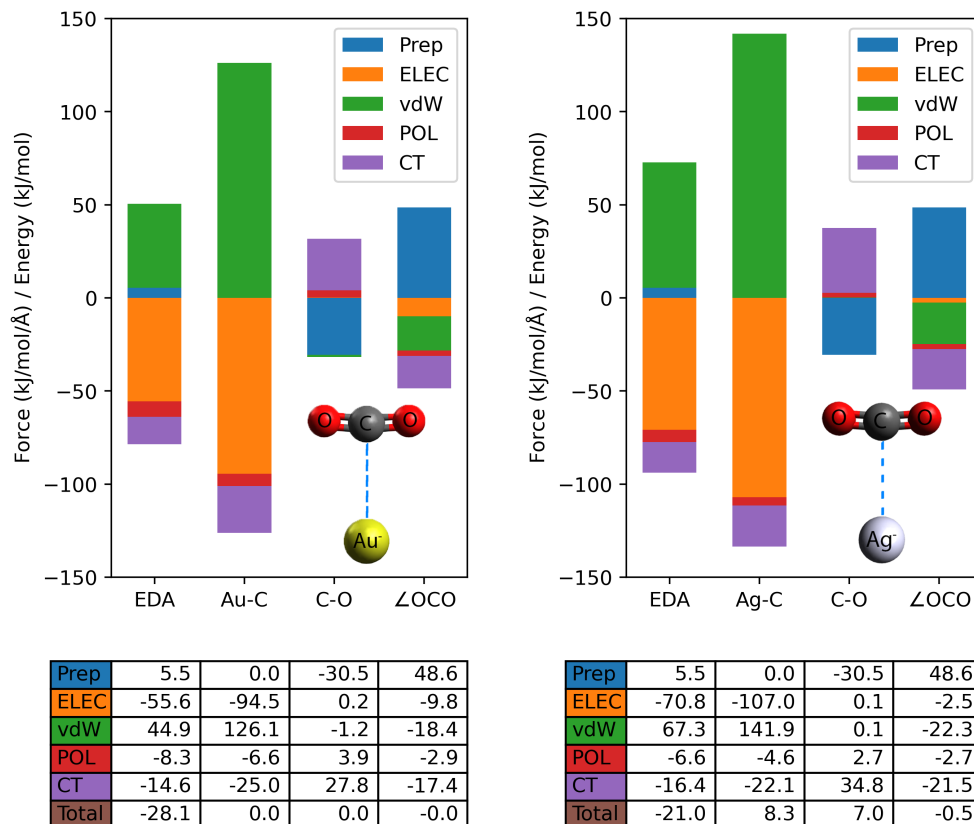
18

Prep	5.5	0.0	-30.5	48.6
ELEC	-55.6	-94.5	0.2	-9.8
vdW	44.9	126.1	-1.2	-18.4
POL	-8.3	-6.6	3.9	-2.9
CT	-14.6	-25.0	27.8	-17.4
Total	-28.1	0.0	0.0	-0.0

Prep	5.5	0.0	-30.5	48.6
ELEC	-70.8	-107.0	0.1	-2.5
vdW	67.3	141.9	0.1	-22.3
POL	-6.6	-4.6	2.7	-2.7
CT	-16.4	-22.1	34.8	-21.5
Total	-21.0	8.3	7.0	-0.5

Figure 8: Comparison of the EDA components (in kJ/mol) and the decomposed forces (in kJ/mol/Å) in internal coordinates for physisorbed $Au^- \cdots CO_2$ (left panel) and $Ag^- \cdots CO_2$ (right panel) complexes, both evaluated at the nuclear coordinates optimized for $Au^- \cdots CO_2$. The energies and forces are decomposed into preparation (Prep), electrostatics (ELEC), van der Waals (vdW), polarization (POL), and charge transfer (CT), and the total intermolecular interaction (Total). The table summarizes the same data with additional significant figures.

We first discuss the physisorption results shown in Fig. 8. The larger size of Ag^- versus Au^- results in a more attractive electrostatic interaction as well as stronger Pauli repulsion in the van der Waals term, with no significant difference in polarization and charge transfer terms. As we use the optimized $Au^- \cdots CO_2$ nuclear coordinates, the net force along each internal coordinate is exactly zero for the $Au^- \cdots CO_2$ complex. Thus inspection of the FDA reveals an exact force balance. Along the $Au-C$ coordinate, van der Waals repulsion is primarily balanced by electrostatics, with small contributions from polarization and CT also favoring shorter bonds. The fact that those latter contributions are so small indicates that CO_2 is scarcely activated, consistent with the near linearity of its optimized geometry. The preparation force favors removing the slight lengthening of the CO bond and very slight bending of the CO_2. In opposition, the drive for CO bond lengthening comes almost entirely from CT, while van der Waals and CT both favor increased angle bending. Comparing $Ag^- \cdots CO_2$ against $Au^- \cdots CO_2$ shows relatively subtle differences associated with the stronger Pauli repulsion forces in the Ag system, which favor longer $Ag-C$ separation, and

extension of the C–O distance as a result of its stronger CT (due to better donor-acceptor overlap, as well as Ag^- being a stronger Lewis base). Finally, as regards the physical driving forces behind the physisorbed complex, both EDA and FDA reveal it to be synergy between dispersion (as indicated by the net binding provided by ELEC+vdW), charge transfer, and polarization.

For the chemisorbed $Au^- - CO_2$ and $Ag^- - CO_2$ species shown in Fig. 9, at the coordinates of the optimized $Au^- - CO_2$ complex, there is a binding energy difference of 24 kJ/mol in favor of the Au complex. Note that the scale for Fig. 9 is 10 times larger than for the physisorbed structures given in Fig. 8. By far the dominant driving force behind the chemisorption geometry is charge transfer. The smaller gold anion exhibits stronger binding from electrostatics, polarization, and charge transfer as well as more repulsive van der Waals interaction compared to the more diffuse silver anion. Despite the lower ionization energy of Ag^- vs. Au^-, the compactness of the gold anion makes charge transfer in $Au^- - CO_2$ significantly more attractive than that in $Ag^- - CO_2$ in which the anion is more diffuse. Accordingly, FDA on $Ag^- - CO_2$ shows a net force for Ag–C elongation. Turning to FDA within the CO_2 subunit, CT (elongation) vs. Prep (contraction) determine the net force on the C–O bond. On the other hand, the net ∠OCO force displays an interesting synergy between the van der Waals repulsion and charge transfer (both favoring bending), versus the preparation force (favoring linearization). To sum up, the compactness of the gold versus silver anion trumps the stronger Lewis basicity of the silver anion in leading to much stronger chemisorption in the Au complex.
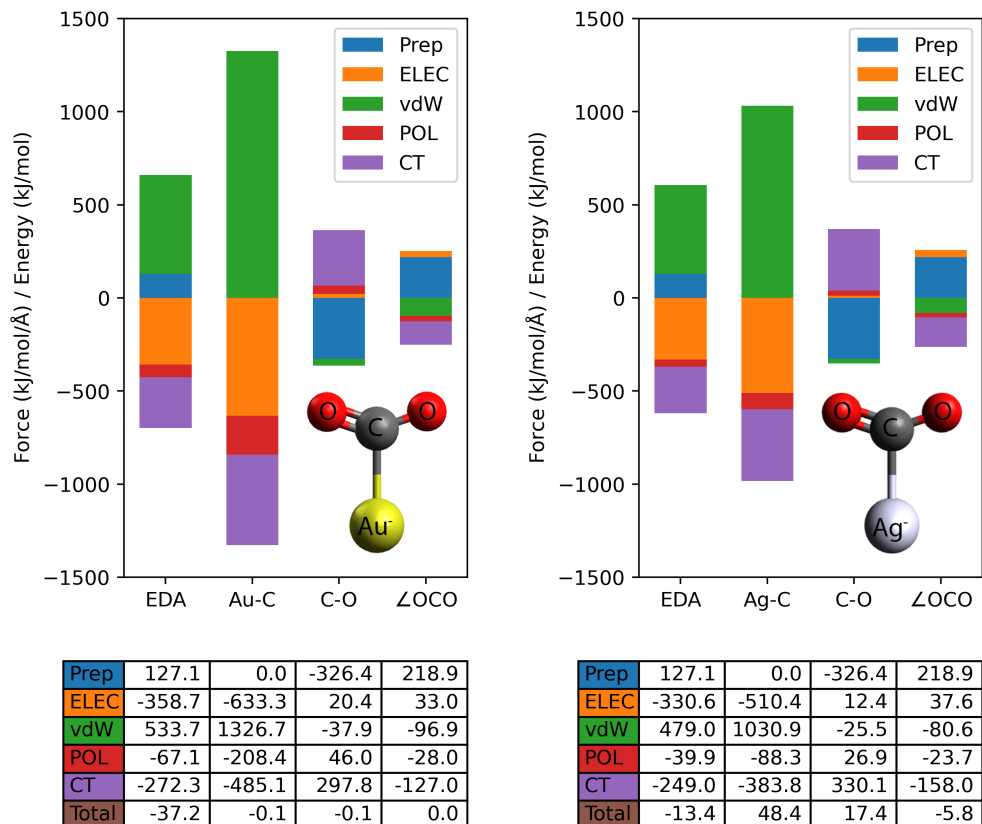
Figure 9: Comparison of the EDA components (in kJ/mol) and the decomposed forces (in kJ/mol/Å) in internal coordinates for chemisorbed $Au^- - CO_2$ (left panel) and $Ag^- - CO_2$ (right panel) complexes, both evaluated at the nuclear coordinates optimized for $Au^- - CO_2$. The energies and forces are decomposed into preparation (Prep), electrostatics (ELEC), van der Waals (vdW), polarization (POL), and charge transfer (CT), and the total intermolecular interaction (Total). The table summarizes the same data with additional significant figures.

4 Conclusions

We have reported theory, implementation, and model applications of an extension to the adiabatic energy decomposition analysis[43] to perform force decomposition analysis of the force components obtained from an EDA method. In particular, the variational absolutely localized molecular orbital EDA (ALMO-EDA) approach[38] is used to analyze Kohn-Sham density functional theory calculations on molecular complexes by differentiating key intermediate energies associated with each non-bonded term. The result is a more information-rich vector of how the different physical driving forces of intermolecular interactions affect each atomic or internal coordinate force within a complex. We expect that our FDA approach can be readily applied to other variational EDA schemes and extended to other molecular properties besides nuclear forces.

More specifically, the net force on either each atom or each internal coordinate of a molecular complex is decomposed into the following physically interpretable contributions.

21

1. A preparation force (Prep), which results from deforming a fragment optimized in isolation to its geometry in the complex. The Prep force will always favor restoring the fragment to its isolated geometry.

2. Forces associated with quasi-classical electrostatics (ELEC), and van der Waals (vdW) interactions (including attractive dispersion and repulsive Pauli interactions) are obtained which sum to the net force resulting from the frozen interaction energy[65] of the ALMO-EDA method. For strongly interacting complexes ELEC and vdW forces are strong and opposite in sign, and it can be advantageous to instead examine the frozen force.

3. Forces associated with the polarization (POL) of the complex,[64] as described by the self-consistent field for molecular interactions (SCF-MI) approach[59–63] in the basis of fragment atomic orbitals.

4. Forces associated with charge delocalization or charge transfer[66,102] between the fragments comprising the complex, which represent the final increment to obtain the total forces.

The model applications presented here are of some intrinsic interest, as well as serving to illustrate the future utility of the FDA for more advanced problems. We presented three sets of examples:

1. We used FDA to examine the Na^+H_2O and Cl^-H_2O complexes, keeping H_2O constrained to its free-molecule geometry. The resulting force balance along the intermolecular distance revealed a greater role for CT in the chloride complex. The net forces within the water molecule showed the role of different components on the intermolecular interaction in distorting the geometry.

2. To illustrate the potential value of FDA to the advanced force field development community, we assessed the fidelity of contributions to the MB-UCB water force field against the FDA components on snapshots of the water dimer. The results showed very good performance for the total atomic forces, and particularly good performance for the center of mass force decompositions, whose RMSD vs FDA components was smaller than the total RMSD.

3. The FDA was also employed to analyze the physisorbed and chemisorbed complexes formed between Au^- and CO_2, and to compare them against the corresponding Ag^-CO_2 complexes. The results showed that while Ag^- is a stronger electron donor than Au^-, the smaller size of Au^- is crucial to the stronger chemisorption of CO_2 to it.

Conflicts of Interest

MHG is a part-owner of Q-Chem Inc, whose software was used for all developments and calculations reported here.

Acknowledgements

References

(1) Liu, S. Y.; Dykstra, C. E. A theory of vibrational transition frequency shifts due to hydrogen bonding. *J. Phys. Chem.* **1986**, *90*, 3097–3103.

(2) Huisken, F.; Kaloudis, M.; Vigasin, A. A. Vibrational frequency shifts caused by weak intermolecular interactions. *Chem. Phys. Lett.* **1997**, *269*, 235–243.

(3) Lalanne, P.; Tassaing, T.; Danten, Y.; Cansell, F.; Tucker, S. C.; Besnard, M. CO 2-Ethanol Interaction Studied by Vibrational Spectroscopy in Supercritical CO 2. *J. Phys. Chem. A* **2004**, *108*, 2617–2624.

(4) Fried, S. D.; Boxer, S. G. Measuring electric fields and noncovalent interactions using the vibrational stark effect. *Acc. Chem. Res.* **2015**, *48*, 998–1006.

(5) Wang, C.; Danovich, D.; Shaik, S.; Mo, Y. A unified theory for the blue-and red-shifting phenomena in hydrogen and halogen bonds. *J. Chem. Theory Comput.* **2017**, *13*, 1626–1637.

(6) Mao, Y.; Head-Gordon, M. Probing blue-shifting hydrogen bonds with adiabatic energy decomposition analysis. *J. Phys. Chem. Lett.* **2019**, *10*, 3899–3905.

(7) Baiz, C. R.; Błasiak, B.; Bredenbeck, J.; Cho, M.; Choi, J.-H.; Corcelli, S. A.; Dijkstra, A. G.; Feng, C.-J.; Garrett-Roe, S.; Ge, N.-H. et al. Vibrational Spectroscopic Map, Vibrational Spectroscopy, and Intermolecular Interaction. *Chem. Rev.* **2020**, *120*, 7152–7218.

(8) Loew, L. M.; Simpson, L.; Hassner, A.; Alexanian, V. An unexpected blue shift caused by differential solvation of a chromophore oriented in a lipid bilayer. *J. Am. Chem. Soc.* **1979**, *101*, 5439–5440.

(9) Fleming, G. R.; Cho, M. Chromophore-Solvent Dynamics. *Annu. Rev. Phys. Chem.* **1996**, *47*, 109–134.

(10) Pieper, J.; Rätsep, M.; Irrgang, K. D.; Freiberg, A. Chromophore-chromophore and chromophore-protein interactions in monomeric light-harvesting complex II of green plants studied by spectral hole burning and fluorescence line narrowing. *J. Phys. Chem. B* **2009**, *113*, 10870–10880.

(11) Rockwell, N. C.; Lagarias, J. C. A Brief History of Phytochromes. *ChemPhysChem* **2010**, *11*, 1172–1180.

(12) Kwon, M. S.; Lee, D.; Seo, S.; Jung, J.; Kim, J. Tailoring Intermolecular Interactions for Efficient Room-Temperature Phosphorescence from Purely Organic Materials in Amorphous Polymer Matrices. *Angew. Chemie* **2014**, *126*, 11359–11363.

(13) González, R.; Mroginski, M. A. Fully Quantum Chemical Treatment of Chromophore-Protein Interactions in Phytochromes. *J. Phys. Chem. B* **2019**, *123*, 9819–9830.

(14) Chen, B.; Huang, W.; Su, H.; Miao, H.; Zhang, X.; Zhang, G. An Unexpected Chromophore–Solvent Reaction Leads to Bicomponent Aggregation-Induced Phosphorescence. *Angew. Chemie - Int. Ed.* **2020**, *59*, 10023–10026.

(15) Kramer, W. W.; McCrory, C. C. Polymer coordination promotes selective CO2 reduction by cobalt phthalocyanine. *Chem. Sci.* **2016**, *7*, 2506–2515.

(16) Nichols, E. M.; Derrick, J. S.; Nistanaki, S. K.; Smith, P. T.; Chang, C. J. Positional effects of second-sphere amide pendants on electrochemical CO 2 reduction catalyzed by iron porphyrins. *Chem. Sci.* **2018**, *9*, 2952–2960.

(17) Zhou, H.; Zou, X.; Wu, X.; Yang, X.; Li, J. Coordination Engineering in Cobalt-Nitrogen-Functionalized Materials for CO2 Reduction. *J. Phys. Chem. Lett.* **2019**, *10*, 6551–6557.

(18) Chen, H.; Guo, X.; Kong, X.; Xing, Y.; Liu, Y.; Yu, B.; Li, Q. X.; Geng, Z.; Si, R.; Zeng, J. Tuning the coordination number of Fe single atoms for the efficient reduction of CO2. *Green Chem.* **2020**, *22*, 7529–7536.

(19) Li, F.; Thevenon, A.; Rosas-Hernández, A.; Wang, Z.; Li, Y.; Gabardo, C. M.; Ozden, A.; Dinh, C. T.; Li, J.; Wang, Y. et al. Molecular tuning of CO2-to-ethylene conversion. *Nature* **2020**, *577*, 509–513.

(20) Wang, Y.; Liu, Y.; Liu, W.; Wu, J.; Li, Q.; Feng, Q.; Chen, Z.; Xiong, X.; Wang, D.; Lei, Y. Regulating the coordination structure of metal single atoms for efficient electrocatalytic CO 2 reduction. *Energy Environ. Sci.* **2020**, *13*, 4609–4624.

(21) Ma, M.; Li, F.; Tang, Q. Coordination environment engineering on nickel single-atom catalysts for CO2electroreduction. *Nanoscale* **2021**, *13*, 19133–19143.

(22) Derrick, J. S.; Loipersberger, M.; Nistanaki, S. K.; Rothweiler, A. V.; Head-Gordon, M.; Nichols, E. M.; Chang, C. J. Templating Bicarbonate in the Second Coordination Sphere Enhances Electrochemical CO2 Reduction Catalyzed by Iron Porphyrins. *J. Am. Chem. Soc.* **2022**, *144*, 11656–11663.

(23) McDaniel, J. G.; Schmidt, J. R. Physically-motivated force fields from symmetry-adapted perturbation theory. *J. Phys. Chem. A* **2013**, *117*, 2053–2066.

(24) McDaniel, J. G.; Schmidt, J. Next-generation force fields from symmetry-adapted perturbation theory. *Annu. Rev. Phys. Chem.* **2016**, *67*, 467–488.

(25) Albaugh, A.; Boateng, H. A.; Bradshaw, R. T.; Demerdash, O. N.; Dziedzic, J.; Mao, Y.; Margul, D. T.; Swails, J.; Zeng, Q.; Case, D. A. et al. Advanced Potential Energy Surfaces for Molecular Simulation. *J. Phys. Chem. B* **2016**, *120*, 9811–9832.

(26) Mao, Y.; Demerdash, O.; Head-Gordon, M.; Head-Gordon, T. Assessing Ion-Water Interactions in the AMOEBA Force Field Using Energy Decomposition Analysis of Electronic Structure Calculations. *J. Chem. Theory Comput.* **2016**, *12*, 5422–5437.

(27) Jing, Z.; Liu, C.; Cheng, S. Y.; Qi, R.; Walker, B. D.; Piquemal, J.-P.; Ren, P. Polarizable force fields for biomolecular simulations: Recent advances and applications. *Ann. Rev. Biophys.* **2019**, *48*, 371–394.

(28) Liu, C.; Piquemal, J.-P.; Ren, P. AMOEBA+ classical potential for modeling molecular interactions. *J. Chem. Theory Comput.* **2019**, *15*, 4122–4139.

(29) Das, A. K.; Urban, L.; Leven, I.; Loipersberger, M.; Aldossary, A.; Head-Gordon, M.; Head-Gordon, T. Development of an Advanced Force Field for Water Using Variational Energy Decomposition Analysis. *J. Chem. Theory Comput.* **2019**, *15*, 5001–5013.

(30) Naseem-Khan, S.; Gresh, N.; Misquitta, A. J.; Piquemal, J. P. Assessment of SAPT and Supermolecular EDA Approaches for the Development of Separable and Polarizable Force Fields. *J. Chem. Theory Comput.* **2021**, *17*, 2759–2774.

(31) Das, A. K.; Liu, M.; Head-Gordon, T. Development of a Many-Body Force Field for Aqueous Alkali Metal and Halogen Ions: An Energy Decomposition Analysis Guided Approach. *J. Chem. Theory Comput.* **2022**, *18*, 953–967.

(32) Phipps, M. J.; Fox, T.; Tautermann, C. S.; Skylaris, C. K. Energy decomposition analysis approaches and their evaluation on prototypical protein-drug interaction patterns. *Chem. Soc. Rev.* **2015**, *44*, 3177–3211.

(33) Mo, Y.; Bao, P.; Gao, J. Energy decomposition analysis based on a block-localized wavefunction and multistate density functional theory. *Phys. Chem. Chem. Phys.* **2011**, *13*, 6760–6775.

(34) Szalewicz, K. Symmetry-adapted perturbation theory of intermolecular forces. *Wiley Interdiscip. Rev. Comput. Mol. Sci.* **2012**, *2*, 254–272.

(35) Jansen, G. Symmetry-adapted perturbation theory based on density functional theory for noncovalent interactions. *Wiley Interdiscip. Rev. Comput. Mol. Sci.* **2014**, *4*, 127–144.

(36) Zhao, L.; von Hopffgarten, M.; Andrada, D. M.; Frenking, G. Energy decomposition analysis. *Wiley Interdiscip. Rev. Comput. Mol. Sci.* **2018**, *8*, e1345.

(37) Su, P.; Tang, Z.; Wu, W. Generalized Kohn-Sham energy decomposition analysis and its applications. *WiRes: Comput. Mol. Sci.* **2020**, *10*, e1460.

(38) Mao, Y.; Loipersberger, M.; Horn, P. R.; Das, A.; Demerdash, O.; Levine, D. S.; Prasad Veccham, S.; Head-Gordon, T.; Head-Gordon, M. From intermolecular interaction energies and observable shifts to component contributions and back again: A tale of variational energy decomposition analysis. *Ann. Rev. Phys. Chem.* **2021**, *72*, 641–666.

(39) Khaliullin, R. Z.; Cobar, E. A.; Lochan, R. C.; Bell, A. T.; Head-Gordon, M. Unravelling the origin of intermolecular interactions using absolutely localized molecular orbitals. *J. Phys. Chem. A* **2007**, *111*, 8753–8765.

(40) Horn, P. R.; Mao, Y.; Head-Gordon, M. Probing non-covalent interactions with a second generation energy decomposition analysis using absolutely localized molecular orbitals. *Phys. Chem. Chem. Phys.* **2016**, *18*, 23067–23079.

(41) Mao, Y.; Levine, D. S.; Loipersberger, M.; Horn, P. R.; Head-Gordon, M. Probing radical–molecule interactions with a second generation energy decomposition analysis of DFT calculations using absolutely localized molecular orbitals. *Phys. Chem. Chem. Phys.* **2020**, *22*, 12867–12885.

(42) Mao, Y.; Loipersberger, M.; Kron, K. J.; Derrick, J. S.; Chang, C. J.; Sharada, S. M.; Head-Gordon, M. Consistent inclusion of continuum solvation in energy decomposition analysis: theory and application to molecular CO 2 reduction catalysts. *Chem. Sci.* **2021**, *12*, 1398–1414.

(43) Mao, Y.; Horn, P. R.; Head-Gordon, M. Energy decomposition analysis in an adiabatic picture. *Phys. Chem. Chem. Phys.* **2017**, *19*, 5944–5958.

(44) Demerdash, O.; Mao, Y.; Liu, T.; Head-Gordon, M.; Head-Gordon, T. Assessing many-body contributions to intermolecular interactions of the AMOEBA force field using energy decomposition analysis of electronic structure calculations. *J. Chem. Phys.* **2017**, *147*, 161721.

(45) Ang, S. J.; Mak, A. M.; Wong, M. W. Nature of halogen bonding involving π-systems, nitroxide radicals and carbenes: a highlight of the importance of charge transfer. *Phys. Chem. Chem. Phys.* **2018**, *20*, 26463–26478.

(46) Thirman, J.; Engelage, E.; Huber, S. M.; Head-Gordon, M. Characterizing the interplay of Pauli repulsion, electrostatics, dispersion and charge transfer in halogen bonding with energy decomposition analysis. *Phys. Chem. Chem. Phys.* **2018**, *20*, 905–915.

(47) Rossomme, E.; Lininger, C. N.; Bell, A. T.; Head-Gordon, T.; Head-Gordon, M. Electronic structure calculations permit identification of the driving forces behind frequency shifts in transition metal monocarbonyls. *Phys. Chem. Chem. Phys.* **2020**, *22*, 781–798.

(48) Loipersberger, M.; Mao, Y.; Head-Gordon, M. Variational Forward-Backward Charge Transfer Analysis Based on Absolutely Localized Molecular Orbitals: Energetics and Molecular Properties. *J. Chem. Theory Comput.* **2020**, *16*, 1073–1089.

(49) Ren, P.; Ponder, J. W. Polarizable Atomic Multipole Water Model for Molecular Mechanics Simulation. *J. Phys. Chem. B* **2003**, *107*, 5933–5947.

(50) Ponder, J. W.; Wu, C.; Ren, P.; Pande, V. S.; Chodera, J. D.; Schnieders, M. J.; Haque, I.; Mobley, D. L.; Lambrecht, D. S.; DiStasio Jr, R. A. et al. Current status of the AMOEBA polarizable force field. *J. Phys. Chem. B* **2010**, *114*, 2549–2564.

(51) Wang, L.-P.; Head-Gordon, T.; Ponder, J. W.; Ren, P.; Chodera, J. D.; Eastman, P. K.; Martinez, T. J.; Pande, V. S. Systematic improvement of a classical molecular model of water. *J. Phys. Chem. B* **2013**, *117*, 9956–9972.

(52) Huang, J.; Lopes, P. E. M.; Roux, B.; MacKerell, A. D. Recent Advances in Polarizable Force Fields for Macromolecules: Microsecond Simulations of Proteins Using the Classical Drude Oscillator Model. *J. Phys. Chem. Lett.* **2014**, *5*, 3144–3150.

(53) Laury, M. L.; Wang, L.-P.; Pande, V. S.; Head-Gordon, T.; Ponder, J. W. Revised parameters for the AMOEBA polarizable atomic multipole water model. *J. Phys. Chem. B* **2015**, *119*, 9423–9437.

(54) Inakollu, V. S.; Geerke, D. P.; Rowley, C. N.; Yu, H. Polarisable force fields: what do they add in biomolecular simulations? *Curr. Opin. Struct. Biol.* **2020**, *61*, 182–190.

(55) Chung, M. K. J.; Wang, Z.; Rackers, J. A.; Ponder, J. W. Classical Exchange Polarization: An Anisotropic Variable Polarizability Model. *J. Phys. Chem. B* **2022**,

(56) Wilson, E. B. Some Mathematical Methods for the Study of Molecular Vibrations. *J. Chem. Phys.* **1941**, *9*, 76–84.

(57) Seki, T.; Chiang, K. Y.; Yu, C. C.; Yu, X.; Okuno, M.; Hunger, J.; Nagata, Y.; Bonn, M. The bending mode of water: A powerful probe for hydrogen bond structure of aqueous systems. 2020; `https://pubs.acs.org/doi/full/10.1021/acs.jpclett.0c01259`.

(58) Horn, P. R.; Head-Gordon, M. Alternative definitions of the frozen energy in energy decomposition analysis of density functional theory calculations. *J. Chem. Phys.* **2016**, *144*, 84118.

(59) Stoll, H.; Wagenblast, G.; Preuß, H. On the use of local basis sets for localized molecular orbitals. *Theor. Chim. Acta* **1980**, *57*, 169–178.

(60) Gianinetti, E.; Vandoni, I.; Famulari, A.; Raimondi, M. Extension of the SCF-MI Method to the Case of K Fragments one of which is an Open-Shell System. *Adv. Quantum Chem.* **1998**, *31*, 251–266.

(61) Nagata, T.; Takahashi, O.; Saito, K.; Iwata, S. Basis set superposition error free self-consistent field method for molecular interaction in multi-component systems: Projection operator formalism. *J. Chem. Phys.* **2001**, *115*, 3553–3560.

(62) Khaliullin, R. Z.; Head-Gordon, M.; Bell, A. T. An efficient self-consistent field method for large systems of weakly interacting components. *J. Chem. Phys.* **2006**, *124*.

(63) Horn, P. R.; Sundstrom, E. J.; Baker, T. A.; Head-Gordon, M. Unrestricted absolutely localized molecular orbitals for energy decomposition analysis: Theory and applications to intermolecular interactions involving radicals. *J. Chem. Phys.* **2013**, *138*, 134119.

(64) Horn, P. R.; Head-Gordon, M. Polarization contributions to intermolecular interactions revisited with fragment electric-field response functions. *J. Chem. Phys.* **2015**, *143*, 114111.

(65) Horn, P. R.; Mao, Y.; Head-Gordon, M. Defining the contributions of permanent electrostatics, Pauli repulsion, and dispersion in density functional theory calculations of intermolecular interaction energies. *J. Chem. Phys.* **2016**, *144*, 114107.

(66) Mao, Y.; Ge, Q.; Horn, P. R.; Head-Gordon, M. On the Computational Characterization of Charge-Transfer Effects in Noncovalently Bound Molecular Complexes. *J. Chem. Theory Comput.* **2018**, *14*, 2401–2417.

(67) Das, A. K.; Demerdash, O. N.; Head-Gordon, T. Improvements to the AMOEBA force field by introducing anisotropic atomic polarizability of the water molecule. *Journal of Chemical Theory and Computation* **2018**, *14*, 6722–6733.

(68) Piquemal, J.; Gresh, N.; Giessner-Prettre, C. Improved formulas for the calculation of the electrostatic contribution to the intermolecular interaction energy from multipolar expansion of the electronic distribution. *J. Phys. Chem. A* **2003**, *107*, 10353–10359.

(69) Thole, B. T. Molecular polarizabilities calculated with a modified dipole interaction. *Chem. Phys.* **1981**, *59*, 341–350.

(70) Wang, L.-P.; Chen, J.; Van Voorhis, T. Systematic parametrization of polarizable force fields from quantum chemistry data. *J. Chem. Theory Comput.* **2013**, *9*, 452–460.

(71) Albaugh, A.; Demerdash, O.; Head-Gordon, T. An efficient and stable hybrid extended Lagrangian/self-consistent field scheme for solving classical mutual induction. *J. Chem. Phys.* **2015**, *143*, 174104.

(72) Albaugh, A.; Head-Gordon, T. A New Method for Treating Drude Polarization in Classical Molecular Simulation. *J. Chem. Theo. Comp.* **2017**, *13*, 5207–5216.

(73) Deng, S.; Wang, Q.; Ren, P. Estimating and modeling charge transfer from the SAPT induction energy. *J. Comput. Chem.* **2017**, *38*, 2222–2231.

(74) Halgren, T. Representation of van der Waals (vdW) Interactions in Molecular Mechanics Force-Fields - Potential Form, Combination Rules, and vdW Parameters. *J. Am. Chem. Soc.* **1992**, *114*, 7827–7843.

(75) Ponder, J. W.; Case, D. A. *Protein Simulations*; Advances in Protein Chemistry; Academic Press, 2003; Vol. 66; pp 27 – 85.

(76) Epifanovsky, E.; Gilbert, A. T. B.; Feng, X.; Lee, J.; Mao, Y.; Mardirossian, N.; Pokhilko, P.; White, A. F.; Coons, M. P.; Dempwolff, A. L. et al. Software for the frontiers of quantum chemistry: An overview of developments in the Q-Chem 5 package. *J. Chem. Phys.* **2021**, *155*, 084801.

(77) Chai, J.-D.; Head-Gordon, M. Long-range corrected hybrid density functionals with damped atom–atom dispersion corrections. *Phys. Chem. Chem. Phys.* **2008**, *10*, 6615–6620.

(78) Rappoport, D.; Furche, F. Property-optimized Gaussian basis sets for molecular response calculations. *J. Chem. Phys.* **2010**, *133*, 134105.

(79) Mardirossian, N.; Head-Gordon, M. ωb97X-V: A 10-parameter, range-separated hybrid, generalized gradient approximation density functional with nonlocal correlation, designed by a survival-of-the-fittest strategy. *Phys. Chem. Chem. Phys.* **2014**, *16*, 9904–9924.

(80) Andrae, D.; Häußermann, U.; Dolg, M.; Stoll, H.; Preuß, H. Energy-adjusted ab initio pseudopotentials for the second and third row transition elements. *Theor. Chim. Acta* **1990**, *77*, 123–141.

(81) Gill, P. M.; Johnson, B. G.; Pople, J. A. A standard grid for density functional calculations. *Chem. Phys. Lett.* **1993**, *209*, 506–512.

(82) Pulay, P.; Fogarasi, G. Geometry optimization in redundant internal coordinates. *J. Chem. Phys.* **1992**, *96*, 2856–2860.

(83) Bakken, V.; Helgaker, T. The efficient optimization of molecular geometries using redundant internal coordinates. *J. Chem. Phys.* **2002**, *117*, 9160–9174.

(84) Ramos-Cordoba, E.; Lambrecht, D. S.; Head-Gordon, M. Charge-transfer and the hydrogen bond: Spectroscopic and structural implications from electronic structure calculations. *Faraday Discuss.* **2011**, *150*, 345–362.

(85) Weinhold, F. Resonance character of hydrogen-bonding interactions in water and other H-bonded species. *Adv. protein Chem.* **2005**, *72*, 121–155.

(86) Weinhold, F.; Klein, R. A. What is a hydrogen bond? Mutually consistent theoretical and experimental criteria for characterizing H-bonding interactions. *Mol. Phys.* **2012**, *110*, 565–579.

(87) Khaliullin, R. Z.; Bell, A. T.; Head-Gordon, M. Electron donation in the water-water hydrogen bond. *Chem. - A Eur. J.* **2009**, *15*, 851–855.

(88) Ronca, E.; Belpassi, L.; Tarantelli, F. A quantitative view of charge transfer in the hydrogen bond: the water dimer case. *ChemPhysChem* **2014**, *15*, 2682–2687.

(89) Stone, A. J. Natural bond orbitals and the nature of the hydrogen bond. *J. Phys. Chem. A* **2017**, *121*, 1531–1534.

(90) Wang, L.-P.; Martinez, T. J.; Pande, V. S. Building force fields: An automatic, systematic, and reproducible approach. *J. Phys. Chem. Lett.* **2014**, *5*, 1885–1891.

(91) Haghighatlari, M.; Li, J.; Heidar-Zadeh, F.; Liu, Y.; Guan, X.; Head-Gordon, T. Learning to Make Chemical Predictions: The Interplay of Feature Representation, Data, and Machine Learning Methods. *Chem* **2020**, *6*, 1527–1542.

(92) Haghighatlari, M.; Li, J.; Guan, X.; Zhang, O.; Das, A.; Stein, C. J.; Heidar-Zadeh, F.; Liu, M.; Head-Gordon, M.; Bertels, L. et al. NewtonNet: a Newtonian message passing network for deep learning of interatomic potentials and forces. *Digit. Discov.* **2022**, *1*, 333–343.

(93) Akin-Ojo, O.; Song, Y.; Wang, F. Developing ab initio quality force fields from condensed phase quantum-mechanics/molecular-mechanics calculations through the adaptive force matching method. *J. Chem. Phys.* **2008**, *129*, 064108.

(94) Jin, S.; Hao, Z.; Zhang, K.; Yan, Z.; Chen, J. Advances and challenges for the electrochemical reduction of CO_2 to CO: from fundamentals to industrialization. *Ang. Chem.* **2021**, *133*, 20795–20816.

(95) Freund, H.-J.; Meijer, G.; Scheffler, M.; Schlögl, R.; Wolf, M. CO oxidation as a prototypical reaction for heterogeneous processes. *Ang. Chem. Int. Ed.* **2011**, *50*, 10064–10094.

(96) Kimble, M. L.; Castleman, A. W.; Mitrić, R.; Bürgel, C.; Bonacic-Koutecky, V. Reactivity of Atomic Gold Anions toward Oxygen and the Oxidation of CO: Experiment and Theory. *J. Am. Chem. Soc.* **2004**, *126*, 2526–2535.

(97) Boese, A. D.; Schneider, H.; Glöß, A. N.; Weber, J. M. The infrared spectrum of Au -·CO 2. *J. Chem. Phys.* **2005**, *122*.

(98) Knurr, B. J.; Weber, J. M. Solvent-driven reductive activation of carbon dioxide by gold anions. *J. Am. Chem. Soc.* **2012**, *134*, 18804–18808.

(99) Zhang, X.; Lim, E.; Kim, S. K.; Bowen, K. H. Photoelectron spectroscopic and computational study of (M-CO2)- anions, M = Cu, Ag, Au. *J. Chem. Phys.* **2015**, *143*.

(100) Bilodeau, R. C.; Scheer, M.; Haugen, H. K. Infrared laser photodetachment of transition metal negative ions: studies on, and. *J. Phys. B* **1998**, *31*, 3885.

(101) Andersen, T.; Haugen, H. K.; Hotop, H. Binding energies in atomic negative ions: III. *J. Phys. Chem. Ref. Data* **1999**, *28*, 1511–1533.

(102) Veccham, S. P.; Lee, J.; Mao, Y.; Horn, P. R.; Head-Gordon, M. A non-perturbative pairwise-additive analysis of charge transfer contributions to intermolecular interaction energies. *Phys. Chem. Chem. Phys.* **2021**, *23*, 928–943.